



Experiment and dynamic simulation of a solar tower collector system for power generation

Jinli Chen ^{a, b}, Gang Xiao ^{a, *}, Haoran Xu ^a, Xin Zhou ^a, Jiamin Yang ^a, Mingjiang Ni ^a, Kefa Cen ^a

^a State Key Laboratory of Clean Energy Utilization, Zhejiang University, 38 Zheda Road, Hangzhou, 310027, China

^b Shanghai Institute of Space Propulsion, 801 Wanfang Road, Shanghai, 201112, China

ARTICLE INFO

Article history:

Received 26 March 2022

Received in revised form

6 July 2022

Accepted 8 July 2022

Available online 14 July 2022

Keywords:

Solar tower

Heliostat field

Tubular air receiver

Experiment

Dynamic simulation

ABSTRACT

Solar air Brayton cycle is a promising option to adjust the renewable power fluctuation due to its quick load regulation capacity. For the successful design and deployment of the solar air Brayton cycle system, the dynamic operation performance of solar collectors under real operating conditions are of great importance. In this study, experiments of a solar collector consisting of the heliostat field and the air receiver are carried out. Based on the experimental investigation of the operating characteristics for the solar collector, a dynamic model is further developed and well-validated to couple the heliostat field and air receiver. The dynamic performance of the air receiver is studied with various factors, including the DNI change and the receiver heat capacity. The results show that the receiver outlet temperature can reach up to 882 °C with a pressure loss of 7.10 kPa and a thermal power of 132 kW during the experiment. Two operation strategies of the air receiver are compared by carrying out the intraday simulation and the constant-outlet-temperature control strategy is more suitable for fast start-up. The method developed in this paper can serve as an efficient tool for the understanding, design and optimization of solar collectors.

© 2022 Elsevier Ltd. All rights reserved.

1. Introduction

Concentrated Solar Power (CSP) technologies, including the solar trough, linear Fresnel and solar tower are capable to provide stable electricity when coupled with large-scale thermal energy storage devices [1]. Among the CSP systems, the solar tower is especially attractive due to its high concentration ratio of up to 1000 suns [2]. A solar tower can be combined with the gas turbine (solar air Brayton cycle) or the supercritical CO₂ Brayton cycle (solar s-CO₂ Brayton cycle) to enable high efficiency for solar thermal power generation [3]. Due to the high-temperature requirement (usually >800 °C) of the pressured air in the solar air Brayton cycle, the dynamic operation performance of the heliostat field and the receiver of the solar tower system is thus needed for its control strategy development [4].

In recent decades, the measurement of concentrating performance of the heliostat field has been attracting growing attention.

In 2002, Ballestrin [5] proposed a direct heat flux measurement system to detect the concentrated solar power at Plataforma Solar de Almeria (PSA) with high accuracy. Then in 2013, Salome et al. [6] used a high-resolution CCD camera and a diffuse target to detect the concentrated solar flux distribution at THEMIS solar tower. In 2018, Ortega et al. [7] used a Kendall radiometer and a calibration panel to measure the incident power on the solar receiver in Sandia National Labs. It realized the online measurement of the thermal power of incident solar radiation to the receiver. Apart from the experiments, heliostat field simulation mainly includes two methods, namely the Monte Carlo ray-tracing (MCRT) method and the analytical method. The Monte Carlo ray-tracing method, such as MIRVAL [8], SolTrace [9], Tonatiuh [10], are accurate with a sufficient number of cast rays, which is computationally expensive in the case of a large heliostat field. The analytical method, such as Helios [11], UNIZAR [12], HFLCAL [13], can save computational time while the results need validation if possible. In 2015, Alberto et al. [14] developed an analytical method based on the UNIZAR model which was validated by PSA measurements and SolTrace software. This method coupled with the projection method could be used for flat plate and multi-panel cylindrical receiver. In 2018, Collado et al.

* Corresponding author.

E-mail address: xiaogangtianmen@zju.edu.cn (G. Xiao).

[15] also proposed a fast and reliable model of flux distribution on the cylindrical receiver based on the HFLCAL model. The flux distribution on the cylindrical receiver obtained by the above methods can be adopted as the boundary condition of solar receivers [16] and used for the optimization of heliostat field layouts [17] and aiming strategies [18].

Solar air receiver is a key component that transfers concentrated solar radiation into the thermal energy of working fluid [19]. There are two kinds of solar air receivers, namely the volumetric receiver and the tubular receiver [20]. A volumetric air receiver usually employs SiC foam ceramics as the absorber and can heat the air to exceed 1200 °C [21]. However, a quartz window is always needed to work as a pressure seal, causing extra problems [22]. On the other hand, the tubular air receiver suffers from low tube temperature (usually <1000 °C) due to the limitation of metal properties. During the year 2006 and 2010, the SOLHYCO project adopted an air receiver that includes 40 straight tubes with a length of 2.5 m [23], in which the air temperature was heated from 600 °C to 782 °C with a pressure loss of 7.00 kPa and an efficiency of about 40%. In 2016, the SOLUGAS project employed a 10-panel straight-tube solar air receiver with a length of 5 m and an inner diameter of 19.6 mm [24], reaching an annual thermal efficiency of 73% with a pressure loss of 2.25%. The outlet temperature of the receiver was around 720 °C. The previous projects SOLHYCO and SOLUGAS demonstrate the technical feasibility of the solar Brayton technology with tubular air receivers by experiments. These two projects also provide the design and manufacture standards for tubular air receivers. In 2018, a novel bladed receiver was designed and tested by Sandia National Laboratories [25], where the air temperature was up to 500 °C with an efficiency exceeding 50% and a high pressure loss of 10%. Apart from experiments, numerical models of solar receivers can be divided into the detailed model and the simplified model. The detailed model is based on CFD tools, such as ANSYS Fluent, for steady-state analysis and optimization. In 2017, Zou et al. [26] put forward a 3D numerical model with ANSYS 17.0 for a cavity receiver to study the effects of geometric parameters on thermal performance. It provides an example to design a cavity receiver. In 2018, Uzair et al. [27] built a numerical model on a cavity receiver using ANSYS CFX to estimate the convective heat losses. Despite the accurate analysis of the geometry's influence on the heat loss process, the detailed models cost too much computational time, thus not feasible for the on-site analysis of the dynamic performance. The simplified model can be developed based on Matlab/Simulink or Dymola, thus is suitable for dynamic performance analysis of receivers. Xu et al. [28] put forward a 3D transient model of the solar receiver tube to investigate its transient thermal performance, in which the heat transfer inside the receiver tubes and the convective heat losses were calculated by empirical correlations. Samanes et al. [29] also developed a transient model of solar cavity receiver and managed to develop a good control strategy, with which the outlet temperature was maintained stable.

Apart from the above studies that solely focus on the heliostat field or the solar receiver, Xiao et al. [30] integrated the two parts in a comprehensive model using the MCRT method and Finite Volume Method (FVM) for a cylindrical cavity receiver in a parabolic dish. Sara [31] further developed an optical-thermal model of a parabolic dish with a cylindrical cavity receiver using SolTrace software and ANSYS Fluent. Pavlovic [32] carried out the experimental and numerical investigation on a solar collector combined with solar parabolic dish and cavity receiver. Bellos [33] developed an optical and thermal model of cavity receiver for solar dish concentrators. Zhou [34] also put forward a model for a spherical cavity receiver with a parabolic dish. However, the developed models from previous works are all steady-state models with parabolic dishes. It is noted that a solar dish is simple for simulation, while a heliostat

field is much complex and practical. Thus, it is essential to develop a dynamic model based on a real heliostat field and solar receiver, which would be used to investigate the dynamic performance of a solar collector system after careful validation and be employed to check and optimize control strategies.

To fill this research gap, both experimental and simulated methods are adopted to measure and predict the flux density distribution of the heliostat field and the dynamic characteristics of the solar receiver at various operating conditions. HFCAL method and quasi-2D approach are used for the development of heliostat field and solar receiver sub-models, respectively. Relative errors and root mean square error (RMSE) between the model results and experimental data are calculated to evaluate the model accuracy. Guided by the validated model, different operation strategies of the air receiver for the applications in solar thermal power systems are compared and the optimization results are performed. This study can guide the solar tower collector system design of the solar Brayton cycle system.

2. Experimental platform

The experiments are conducted in Qingshanhu Solar Tower Research Center of Zhejiang University of China, as shown in Fig. 1. The research center consists of a solar tower and a heliostat field. The height of the solar tower is 45 m, and the heliostat field has 100 mirrors of 19.5 m², whose reflectivity is 0.94 and surface clearness is 0.95 (supplied by manufacturer).

2.1. Measurement system for flux density distribution

The measurement system for flux density distribution consists of a CCD camera and a Lambertian target plane (shown in Fig. 2). The concentrated solar energy is projected on the target plane, and the grayscale image of flux density distribution is captured by the CCD camera, which is transformed to the relative flux density distribution [36]. There is a water-cooled heat flux gauge placed on the target plane to measure the solar radiation intensity of the reference point which is not very close to the center of the Lambert target plane. Then, the flux density distribution of the whole target plane can be mapped by comparing the reference point value.

2.2. Experimental system for air receiver

The air receiver is mounted at the top window of the solar tower, and Fig. 3 (a) shows the schematic and photographs of the



Fig. 1. Qingshanhu solar tower research center of zhejiang university of China [35].

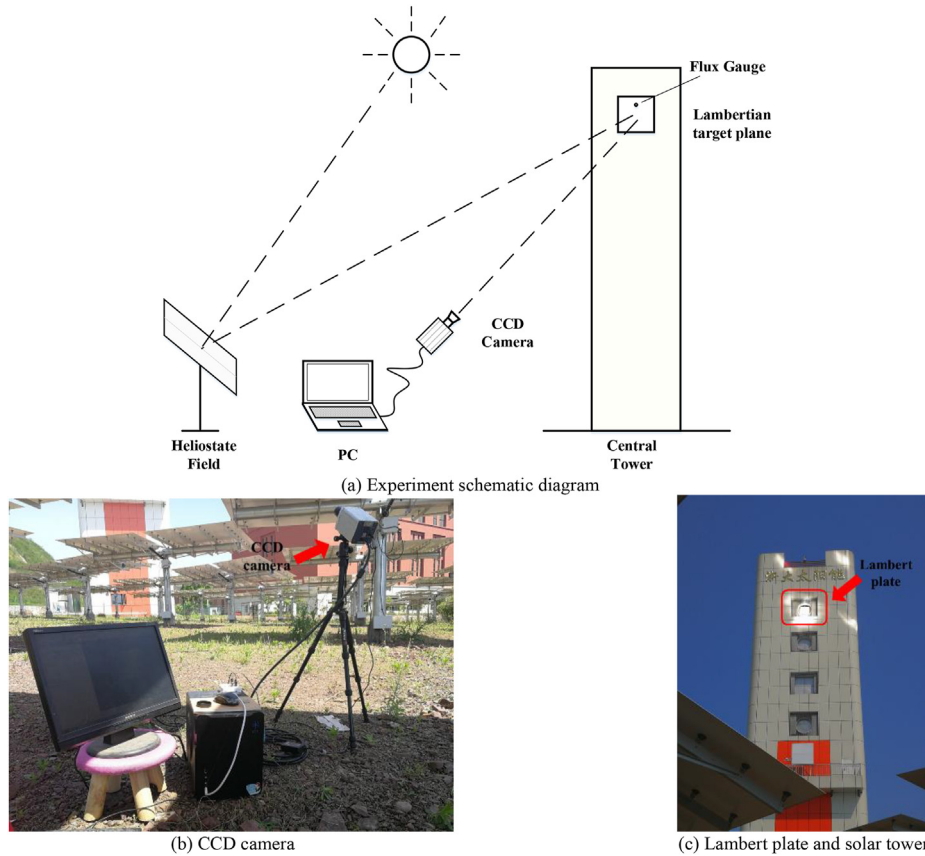


Fig. 2. The experiment of flux density distribution measurement.

experiment system. There is a compressor to supply compressed air, a flowmeter at the receiver inlet to measure the mass flow rate, and a valve at the receiver outlet to control the air pressure. Thermocouples and pressure sensors are arranged at the receiver inlet and outlet. The direct normal irradiance (DNI) is measured by a direct radiation meter.

A cavity air receiver which is shown in Fig. 3 (b) is adopted here due to its lower radiation heat loss compared to the external receiver [37]. The cold air flows through the receiver inlet to the inlet header at the bottom of receiver and flows through the primary heating tubes near the aperture. Then the heated air is mixed in connection header. Finally, the air flows through the secondary heating tubes near insulation and flows out of the receiver through the receiver outlet. The spacing between the adjacent primary heating tubes is about 20 mm–30 mm to ensure leaving enough space for secondary heating tubes absorbing solar radiation.

The designed thermal power of the receiver is 120 kW_{th}. There are three headers for connecting receiver tubes. The inner diameter of the header tube is 113 mm with a thickness of 10 mm. The aperture diameter of the receiver is 800 mm, the outer diameter is 1200 mm with a height of 1244 mm. The cavity receiver is tilted downwards at $\varnothing = 27^\circ$. The receiver tube is made of Inconel 625 with an inner diameter of 12 mm and its thickness is 2.0 mm. The reflectivity of the receiver tube is about 0.124 [38].

3. Dynamic model development

3.1. Simulation on the flux density distribution

The flux density distribution simulation determines how much

solar energy is incident on the receiver, which is the boundary condition for solar receiver simulation.

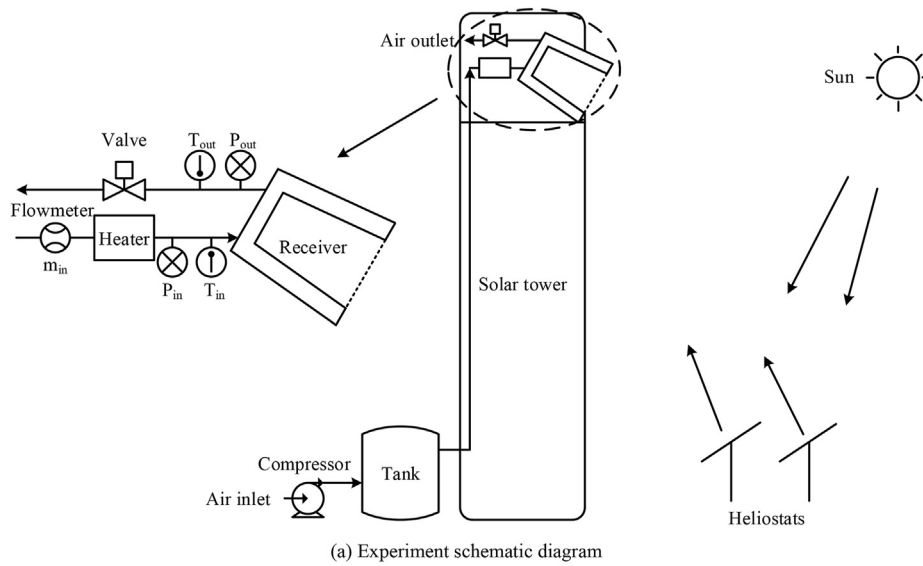
An analytical method is adopted in flux density distribution simulation due to its fast computation speed here. The flux density distribution of each mirror on the receiver aperture plane is calculated using the HFLCAL model with a circular normal distribution. Then, it can be projected to the receiver cavity. The flux density distribution on the receiver aperture plane of one mirror can be calculated [6]:

$$FLUX_m(x, y) = \frac{Pow_m}{2 \cdot \pi \cdot \sigma_m^2} \cdot e^{-\frac{((x-x_{AP})^2 + (y-y_{AP})^2)}{2 \cdot \sigma_m^2}} \quad (1)$$

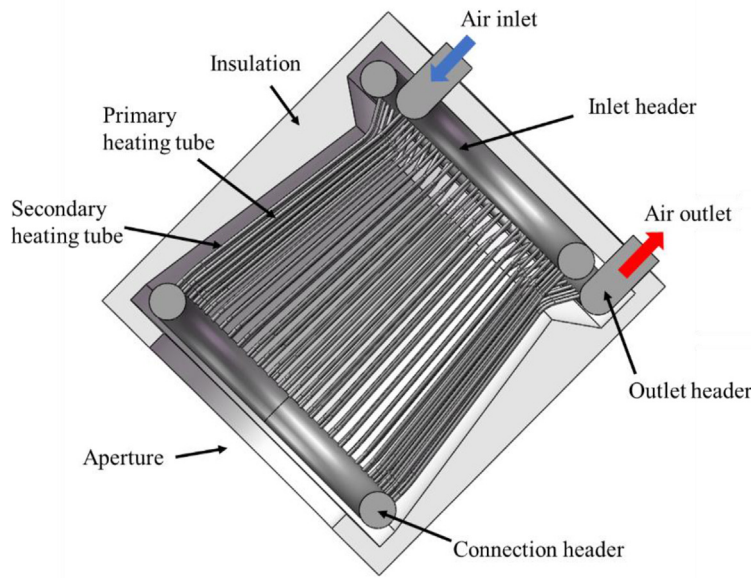
where Pow_m is the total solar power reflected by the mirror; σ_m is the effective deviation and (x_{AP}, y_{AP}) is the coordinate of the ray reflected by the mirror center on the receiver aperture plane. Pow_m can be expressed:

$$Pow_m = I_D \cdot A_m \cdot \eta_{s\&b} \cdot f_{at} \cdot \beta_m \cdot \cos \omega \quad (2)$$

where I_D is the DNI, A_m is the mirror area, $\eta_{s\&b}$ is the shading and blocking efficiency of the mirror, f_{at} is the atmospheric attenuation factor, β_m is the mirror reflectivity and $\cos \omega$ is the cosine efficiency of the mirror. The effective deviation (σ_m) is the convolution of the four errors, namely the sun shape error (σ_{sun}), the beam quality error (σ_{bq}), the astigmatic error (σ_{ast}) and the tracking error (σ_t). The effective deviation can be calculated [39]:



(a) Experiment schematic diagram



(b) Section view of tubular receiver

Fig. 3. Experiment system of air receiver.

$$\sigma_m = \frac{\sqrt{D^2 \cdot (\sigma_{sun}^2 + \sigma_{bq}^2 + \sigma_{ast}^2 + \sigma_t^2)}}{\sqrt{\cos rec}} \quad (3)$$

where D is the distance between the mirror center and the aim point, $\cos rec$ is the cosine of the angle between the ray reflected by the mirror center and the normal to the receiver aperture plane.

Fig. 4 shows the coordinate systems when simulating the flux density distribution. There are three system coordinates: the global coordinate, the heliostat coordinate and the receiver coordinate. The flux density distribution simulation is completed through these coordinate systems and coordinate transformation.

The flux density distribution inside the receiver cavity can be calculated through the projection method [14] based on the flux density distribution on the receiver aperture. The receiver cavity is discretized into several nodes before projection calculation. Then each node is projected into the receiver aperture plane along the opposite direction of the ray reflected from each mirror center.

Finally, the projection nodes within the receiver aperture are calculated. In this way, the solar flux density distribution on the receiver cavity is calculated. To simplify the model calculation, the ray reflection inside the receiver cavity is ignored. Then, the solar flux density distribution on the receiver cavity is set as the boundary condition for receiver simulation.

The shading and blocking of the adjacent mirrors cause some energy loss of the heliostat field. The shading loss occurs when the incoming solar radiation is obstructed by the adjacent mirrors, while the blocking loss occurs when the reflected rays from one mirror are blocked by the nearby mirrors from reaching the receiver. In Fig. 5, the first two mirrors with the highest potential for shadowing (red circles in Fig. 5) are selected for further investigation. Similarly, the mirrors in blue circles have the highest potential for blocking [40].

For shading and blocking efficiency calculation, the potential shadowing and blocking mirrors are projected into the aim mirror plane along the incoming solar radiation direction or the reflected ray direction. Then the overlap area among the shadows of the

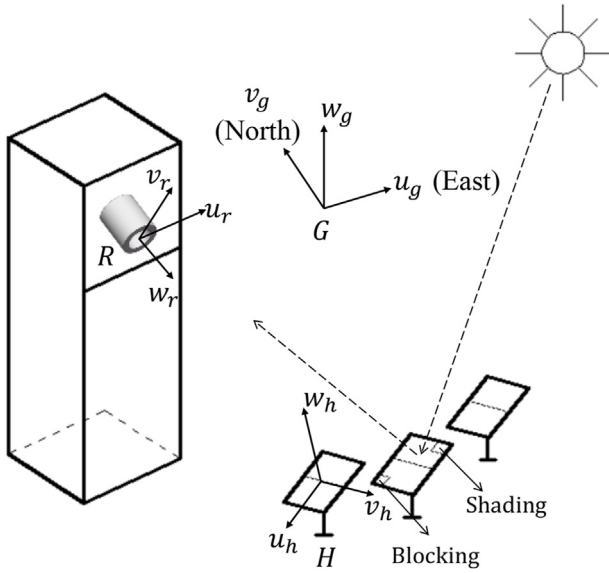


Fig. 4. The coordinate systems for modeling flux density distribution.

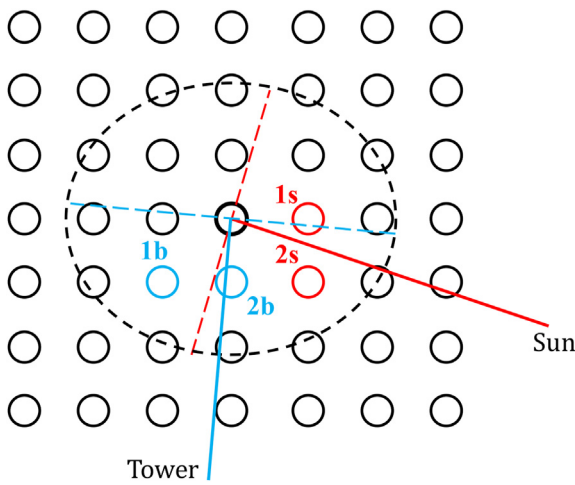


Fig. 5. The diagram to identify the potential shadowing and blocking mirrors.

adjacent mirrors and the aim mirror is calculated. In this way, the shading efficiency and the blocking efficiency of the heliostat field can be obtained.

3.2. Air receiver model

There are two main thermal losses in cavity air receiver, namely the heat losses through the receiver aperture and the insulation layer, as shown in Fig. 6. The heat loss through the receiver aperture Q_{ape} consists of the reflection loss Q_{ref} , convection heat loss Q_{con_ape} and radiation heat loss Q_{rad} , while the heat loss through the insulation layer is mainly the convection heat loss Q_{con_ins} .

For simplification, the effect of wind is not considered in the receiver model. The energy conservation equation of the air receiver can be expressed:

$$Q_{tot} = Q_{abs} + Q_{ape} + Q_{ins} = Q_{abs} + Q_{ref} + Q_{rad} + Q_{con_ape} + Q_{con_ins} \quad (4)$$

where Q_{tot} is the total solar energy incident to the receiver aperture

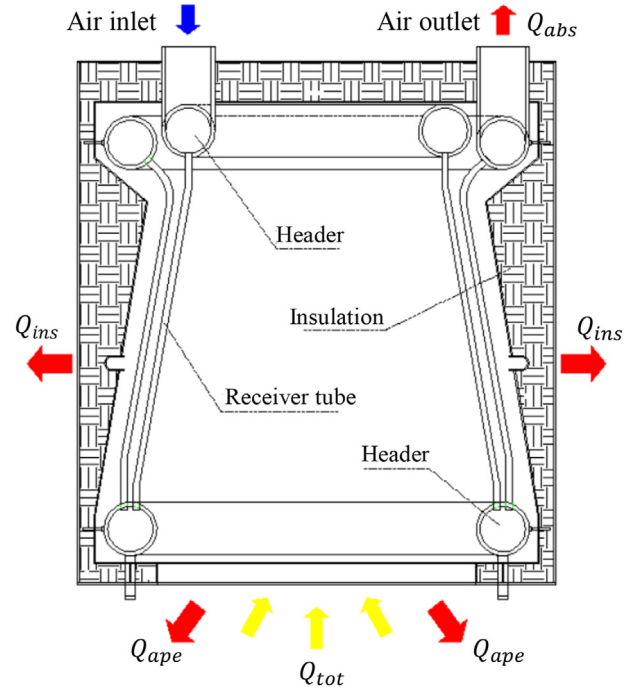


Fig. 6. The energy flow distribution of the air receiver.

which can be determined by the heliostat field simulation, Q_{abs} is the thermal energy absorbed by the working fluid, Q_{ape} is the heat loss through the receiver aperture and Q_{ins} is the heat loss through the insulation layer.

The reflection loss through the receiver aperture Q_{ref} can be calculated using the reflectivity of the receiver cavity which can be expressed:

$$\beta_{ref} = 1 - \frac{\epsilon}{1 - (1 - \epsilon) \cdot (1 - A_{ape}/A_{cav})} \quad (5)$$

In Eq. (5), ϵ is the emissivity of the receiver cavity, A_{ape} is the receiver aperture area, A_{cav} is the receiver cavity area.

The receiver radiation heat loss Q_{rad} through the receiver aperture is calculated using the view factors instead of the empirical equations. Here, the view factors between the receiver cavity wall and the receiver aperture are calculated. The receiver discretization is shown in Fig. 7 (a), the receiver cavity and aperture are discretized for radiation heat loss calculation. The definition of view-factor is shown in Fig. 7 (b) and the calculation of view-factor from surface a to surface b can be expressed:

$$F_{ab} = \frac{\cos(\alpha_a) \cdot \cos(\alpha_b)}{\pi \cdot D_{ab}^2} \cdot dA_b \quad (6)$$

Where α_a and α_b are the respective tilting relative to the line of centers of two surfaces. Then the radiation heat loss from surface a to surface b (Q_{rad_ab}) is calculated as Eq. (7). In this way, the radiation heat loss from the receiver cavity to receiver aperture can be determined.

$$Q_{rad_ab} = F_{ab} \cdot \epsilon \cdot \varphi \cdot ((T_a + 273.15)^4 - (T_b + 273.15)^4) \cdot dA_a \quad (7)$$

where φ is Stefan-Boltzmann constant.

Different empirical equations are adopted for the convection heat loss calculation through receiver aperture. These correlations are shown in Table 1.

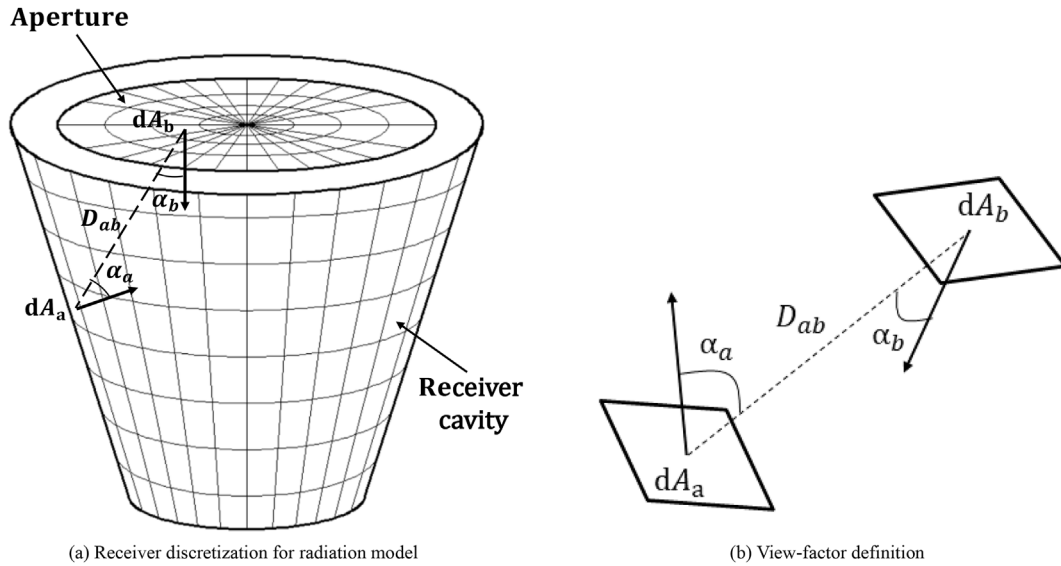


Fig. 7. Receiver discretization and view-factor definition for radiation model.

The convection heat loss through receiver aperture Q_{con_ape} is shown in Eq. (8), where h_{con} is the convective heat transfer coefficient, T_{cav} is the cavity temperature and T_{amb} is the ambient temperature. The convection heat loss through the insulation layer can be calculated the same way.

$$Q_{con_ape} = h_{con} \cdot A_{cav} \cdot (T_{cav} - T_{amb}) \quad (8)$$

For the calculation of thermal energy absorbed by the working fluid, a quasi-2D approach is adopted in the receiver heat transfer calculation among the receiver tube, working fluid and insulation layer (shown in Fig. 8). There are four calculation zones in the receiver heat transfer model. Zone 0 represents the receiver tube wall that is exposed to solar irradiation. Zone 1 represents the working fluid that absorbs the solar energy transferred from zone 0. Zone 2 is the receiver tube wall which is unexposed to solar irradiation. Zone 3 is the insulation layer.

Each zone is divided into several calculation units, the energy conservation equation of each zone can be expressed as:

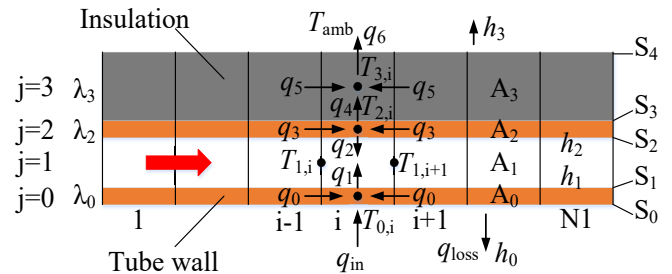


Fig. 8. The receiver calculation model.

$$\frac{\partial(\rho \cdot c_p \cdot T \cdot A)}{\partial t} + \frac{\partial(m \cdot c_p \cdot T)}{\partial x} = \frac{q}{\Delta x} \quad j = 1 \quad (9)$$

$$\frac{\partial(M \cdot c_v \cdot T)}{\partial t} = q \quad j = 0, 2, 3 \quad (10)$$

where M is the mass of each solid unit, q is the heat transfer among

Table 1

The correlations for convection heat loss calculation.

Equation name	Correlations for heat transfer coefficient calculation or Nusselt number calculation	Illustrations
Siebers and Kraabel (SK for short) 1984 [41]	$h_{con} = 0.81 \cdot (T_{cav} - T_{amb})^{0.426} \cdot \left(\frac{A_{tot}}{A_{up}}\right) \cdot \left(\frac{A_{low}}{A_{tot}}\right)^{0.63}$	T_{cav} -the average cavity temperature T_{amb} -the ambient temperature A_{tot} -the total cavity surface area A_{up} -the cavity surface area of the upper lip A_{low} -the cavity surface area of the lower lip
Stine and McDonald (SM for short) 1989 [42]	$Nu_{con} = 0.088 \cdot Gr^{1/3} \cdot \left(\frac{T_{cav} + 273.15}{T_{amb} + 273.15}\right)^{0.18} \cdot (\cos \varphi)^{2.47} \cdot \left(\frac{D_{ape}}{L_{cav}}\right)^s$ $s = 1.12 - 0.98 \cdot \left(\frac{D_{ape}}{L_{cav}}\right)$	φ -the cavity inclination D_{ape} -the diameter of the receiver aperture L_{cav} -the length of the receiver cavity
Paitoonsurikarn and Lovegrove (PL for short) 2006 [43]	$Nu_{con} = 0.0196 \cdot Ra_L^{0.41} \cdot Pr^{0.13} = \frac{h \cdot L_s}{k}$ $L_s = \left \sum_{i=1}^3 a_i \cdot \cos(\varphi + \psi_i)^{b_i} \cdot L_i \right $	a_i, b_i, ψ_i -the constants for the evaluation of the ensemble cavity length scale L_s -the cavity length scale L_1 -the cavity diameter L_2 -the cavity length L_3 -the aperture diameter φ -the cavity inclination

the adjacent units. The forced convection heat transfer between working fluid and stainless-steel pipe is calculated according to the Gnielinski equation [44]. The air property functions adopted in the receiver model are from the library REFPROP. In this way, the thermal energy absorbed by the working fluid and the heat loss through the insulation layer can be calculated. For pressure loss calculation, the pressure loss along the path is calculated through Darcy formula while the local pressure loss is calculated through empirical formula [45].

4. Results and discussions

4.1. Flux density distribution of heliostat field

There is a total of 52 mirrors tested in the heliostat field. The flux density distribution simulation of each case is carried out according to the experimental conditions. Then, the simulation and the experiment results are compared to validate the heliostat field model. The parameters for comparison are the maximum flux density and the total energy collected on the Lambert plate. The comparison results are shown in Fig. 9.

The simulated flux density distribution is more regular than the experiment result. For 7 mirrors, the relative errors of the maximum flux density and the total collected solar energy between experiment and simulation results are 1.09% and 5.23%. For 52 mirrors, these two values are 3.81% and 3.05%, respectively. In this case, the maximum flux density of the experiment is 388 kW/m² when DNI is 750 W/m². The simulation values of the maximum flux density and the total collected solar energy on the Lambert plate are a little higher than the experiment values. Generally, this study shows that the heliostat field model is validated well.

4.2. Operation performance of air receiver

4.2.1. Steady performance

This part presents the steady performance of the air receiver. The experiment data shown in Table 2 is the average value within 10 min for each case. The solar energy incident to the receiver aperture is determined by the heliostat field model.

The thermal efficiency of the air receiver is related to the receiver outlet temperature and air mass flow rate. According to cases 1, 2 and 5, the receiver outlet temperatures are all around

880 °C. When the mass flow rate increases from 0.1064 kg/s to 0.1426 kg/s, the receiver absorbs much more solar energy, thus the thermal efficiency increases from 63.3% to 67.3%.

According to cases 3 and 4, when the air mass flow rate is similar, the higher receiver outlet temperature leads to higher air velocity and higher receiver tube temperature thus causing a higher heat loss and a lower thermal efficiency. It is the same tendency between cases 5 and 6.

The receiver pressure loss is related to the receiver outlet temperature, mass flow rate and inlet pressure. According to cases 2 and 3, the mass flow rate and the inlet pressure are similar. Case 2 has a higher receiver outlet temperature causing a higher pressure loss. Comparing cases 4 and 5, the receiver outlet temperature and the mass flow rate are similar. Case 5 has a higher inlet pressure leading to a lower pressure loss. This is because the higher inlet pressure leading to a larger air density causing a lower airflow velocity, thus causing a smaller pressure drop. Comparing cases 1 and 6, the inlet pressures of both cases are similar. Though the receiver outlet temperature of case 1 is higher, the lower mass flow rate of case 1 causing a lower receiver pressure loss.

During the receiver test, the receiver outlet temperature can reach above 880 °C which is suitable for micro gas turbine operation. Meanwhile, the receiver pressure loss is 0.88% of the inlet pressure when inlet pressure is above 280 kPa. The thermal efficiency and thermal power of the receiver can reach 68.9% and 132 kW, respectively.

4.2.2. Dynamic performance

The influence of different factors variations on receiver performance is investigated, including the mass flow rate, input solar energy and inlet pressure. The experiment data of 29th April and 12th May are discussed here.

Fig. 10 shows the experimental results of the air receiver on 29th April. There are several operation condition changes during the whole test. At position 1 (around 10:35), the air mass flow rate increases from 0.0660 kg/s to 0.1420 kg/s. The pressure loss inside the air receiver increases from 2.56 kPa to 9.26 kPa suddenly. At the same time, the receiver outlet temperature decreases gradually because of the thermal inertia of the air receiver. The duration of receiver outlet temperature decreases from 844 °C (10:35) to 735 °C (11:12) is around 37 min. At around 11:23 (position 2), another 10 mirrors are put into operation. At this time, the total number of

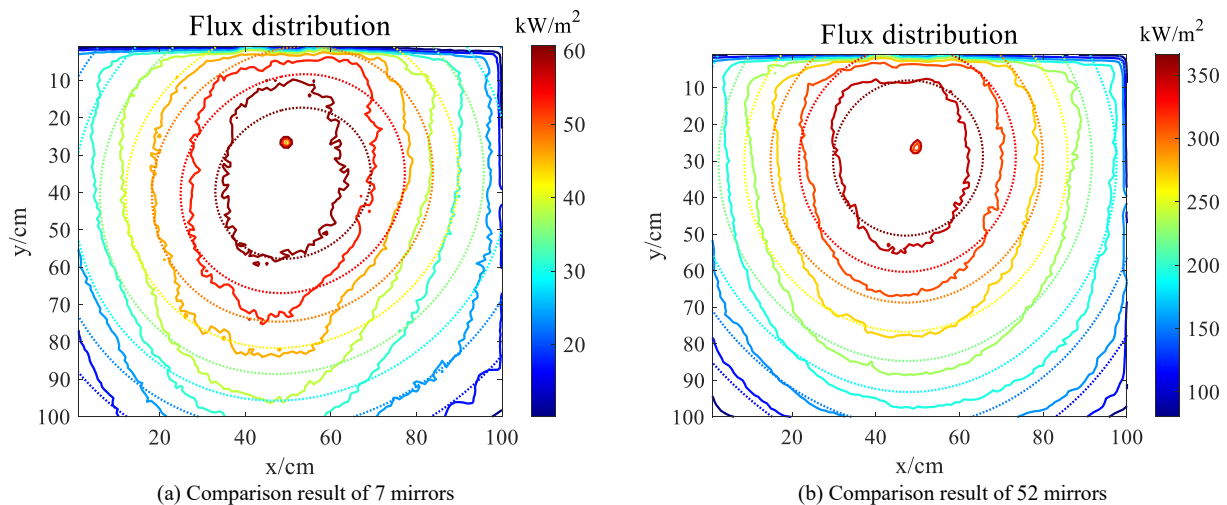


Fig. 9. Comparison results of flux density distribution between experiment (Solid lines) and simulation (Dotted lines).

Table 2
Different steady performance experimental cases.

Case	Testing period	Mirror number	DNI W/m ²	T _{in} °C	T _{out} °C	m kg/s	P _{in} kPa	P _{loss} kPa	Pow _{abs} kW	Pow _{input} kW	Efficiency %
1	April 28 (11:33–11:43)	58	813	26	888	0.1064	284	2.50	100	158	63.3
2	April 28 (12:31–12:41)	58	807	28	882	0.1426	146	7.13	132	196	67.3
3	April 28 (13:28–13:38)	48	773	29	814	0.1418	152	6.37	120	174	68.9
4	April 29 (13:21–13:31)	68	688	36	875	0.1377	163	6.09	126	188	67.0
5	May 12 (11:47–11:57)	49	861	33	884	0.1311	263	3.29	121	183	66.1
6	May 12 (12:53–13:03)	39	852	35	845	0.1295	281	2.86	114	170	67.1

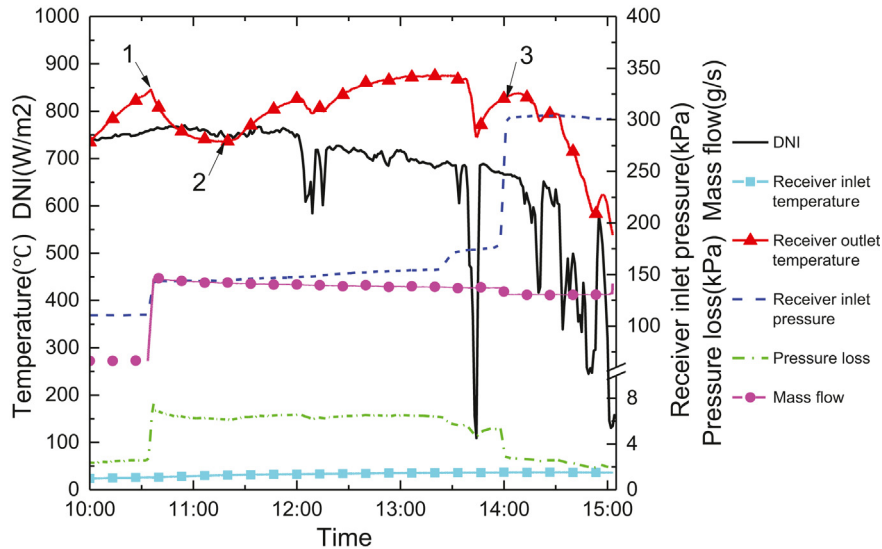


Fig. 10. Experiment performance of solar receiver (29th April).

working mirrors is 68. After putting more mirrors into operation, the receiver outlet temperature increases, and then it changes with DNI fluctuation.

From 13:39 to 13:44, the DNI drops from 632 W/m² to 109 W/m², the receiver outlet temperature decreases from 859 °C to 745 °C. Then, the DNI increases back to 685 W/m² in 2 min. The receiver outlet temperature increases to 838 °C gradually at around 14:07. The temperature dropping rate of the air receiver outlet is much faster than its rising rate. At around 13:59 (position 3), the receiver inlet pressure increases from 174 kPa to 304 kPa by adjusting the valve at the receiver outlet. The pressure loss of airflow decreases from 4.50 kPa to 2.86 kPa immediately.

Fig. 11 shows the experimental results of the air receiver on 12th May. During the test, the heliostat field is adjusted to obtain a constant receiver outlet temperature manually. The adjustment range of receiver outlet temperature is 800 °C–900 °C. At around 11:27 (position 1), 59 mirrors are operating and the receiver outlet temperature reaches 906 °C. To avoid receiver overheating, 10 mirrors are laid flat. The receiver outlet temperature decreases gradually, and then it increases again because of the improvement of heliostat field efficiency near the midday. At position 2, another 10 mirrors are closed causing the receiver outlet temperature to decrease again. At around 15:32 (position 6), the heliostat field is closed, the receiver outlet temperature decreases from 795 °C rapidly.

At the start-up period of the air receiver, the receiver outlet temperature increases from ambient temperature to over 800 °C in 70 min (in 26 min the receiver outlet temperature increases from ambient temperature to 500 °C). During the shut-down period, the receiver outlet temperature decreases from 795 °C to below 100 °C

in 59 min (in 17 min the receiver outlet temperature decreases from 795 °C to 395 °C). When the receiver is working at a high-temperature condition, the receiver outlet temperature is easier to be cooled down than heated up when DNI changes.

The relationship among receiver outlet temperature, air density and pressure loss are shown in Fig. 12. The pressure loss of the air receiver is related to the air average density directly. This is due to the pressure loss of the air receiver is affected by air velocity which is determined by air density. Thus, the lower air average density inside the receiver tube leads to a higher air velocity causing a larger pressure loss.

4.2.3. Model validation

In this part, the receiver model is validated using experimental data, and different equations for convection heat loss calculation are checked. Fig. 13 shows the simulation results of two receiver experiment cases. Three convection heat loss correlations adopted here are SK equation, SM equation and PL equation.

The simulation results indicate that the receiver outlet temperature is more sensitive to mass flow rate than DNI. Fig. 13 shows that the modeling outlet temperature drops immediately when the mass flow rate increases suddenly, while the experimental temperature decreases gradually. This is probably because the mass flow rate change inside the air receiver has a volume effect. Thus, it is relatively lagged compared to the measured value of the receiver inlet.

The RMSE values of receiver outlet temperature between experiment and simulation results using different convection heat loss correlations have been compared.

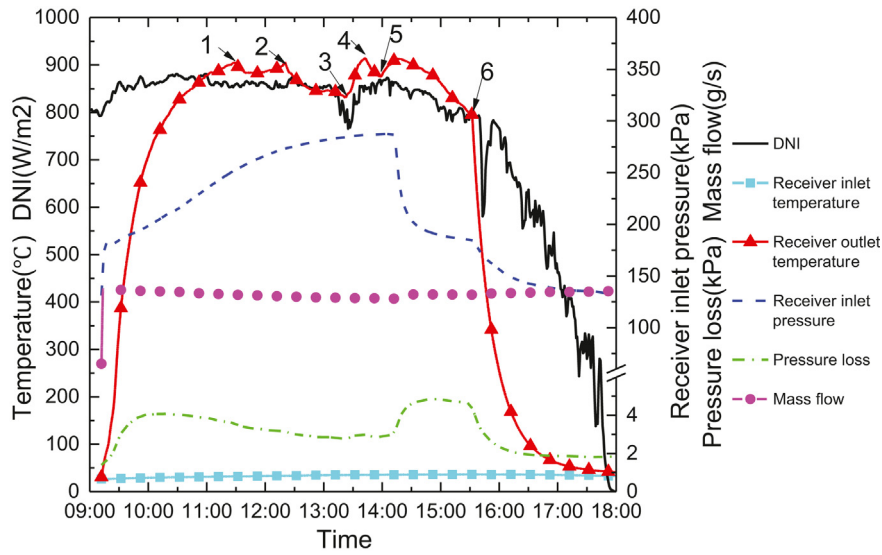


Fig. 11. Experiment performance of air receiver (12th May).

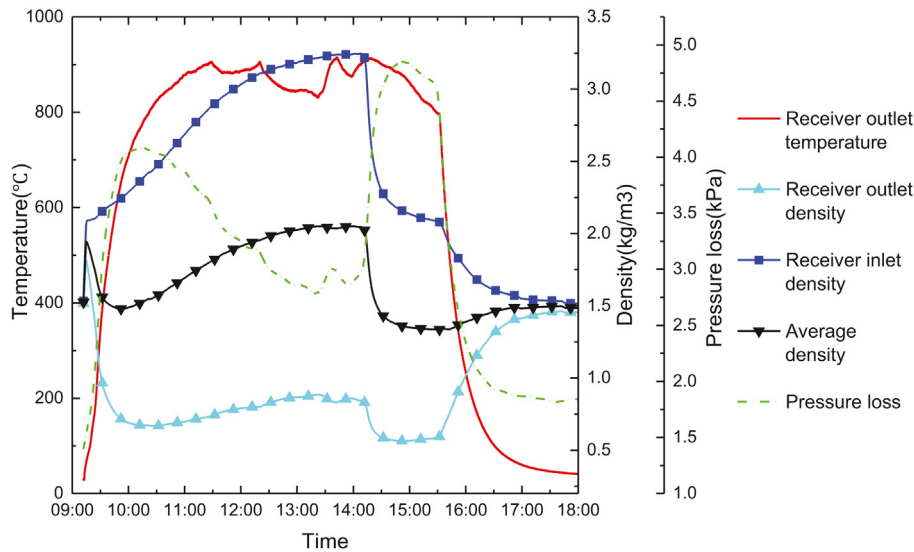


Fig. 12. The relationship among receiver outlet temperature, air density and pressure loss.

$$RMSE = \sqrt{\frac{1}{n_d} \cdot \sum_{i=1}^{n_d} \left(\frac{y_m - y}{y_m} \right)^2} \quad (11)$$

where y_m is the experiment data, y is the simulation data and n_d is the data number. The comparison results are shown in Table 3.

It seems that the PL equation has the best accuracy to calculate the convection heat loss of the air receiver. Thus, the PL equation is adopted for receiver dynamic simulation.

4.3. Further research based on the developed model

4.3.1. Factors affecting receiver dynamic performance

Here the influences of DNI change and receiver heat capacity is investigated on the dynamic performance of air receiver. In this part, the mass flow rate of the air receiver is set at 0.16 kg/s while the inlet temperature is set at 30 °C.

The response of air receiver outlet temperature is shown in Fig. 14 (a) with DNI changes of 200 W/m², 400 W/m², 600 W/m² and 800 W/m². At the beginning of DNI disturbance, the DNI value is 800 W/m², the receiver outlet temperature is 944 °C. After 20 min, the DNI decreases causing a drop in receiver outlet temperature. The larger DNI decreasing value leads to a larger receiver outlet temperature drop as well as a faster temperature decreasing rate. When DNI decreasing value is 800 W/m² (DNI decreases from 800 W/m² to 0 sharply), the receiver outlet temperature drops from 944 °C to 386 °C in 20 min. When this value is 200 W/m², the receiver outlet temperature drop is from 944 °C to 829 °C.

At the beginning of the DNI decrease period, the receiver outlet temperature dropping rate increases from 10.3 °C/min to 41.3 °C/min when DNI decreasing value rises from 200 W/m² to 800 W/m². This is because the larger change in incident energy into the air receiver would cause a faster receiver temperature change. At the beginning of the DNI increase period, the receiver outlet temperature rising rate increases from 7.9 °C/min to 38.2 °C/min when DNI

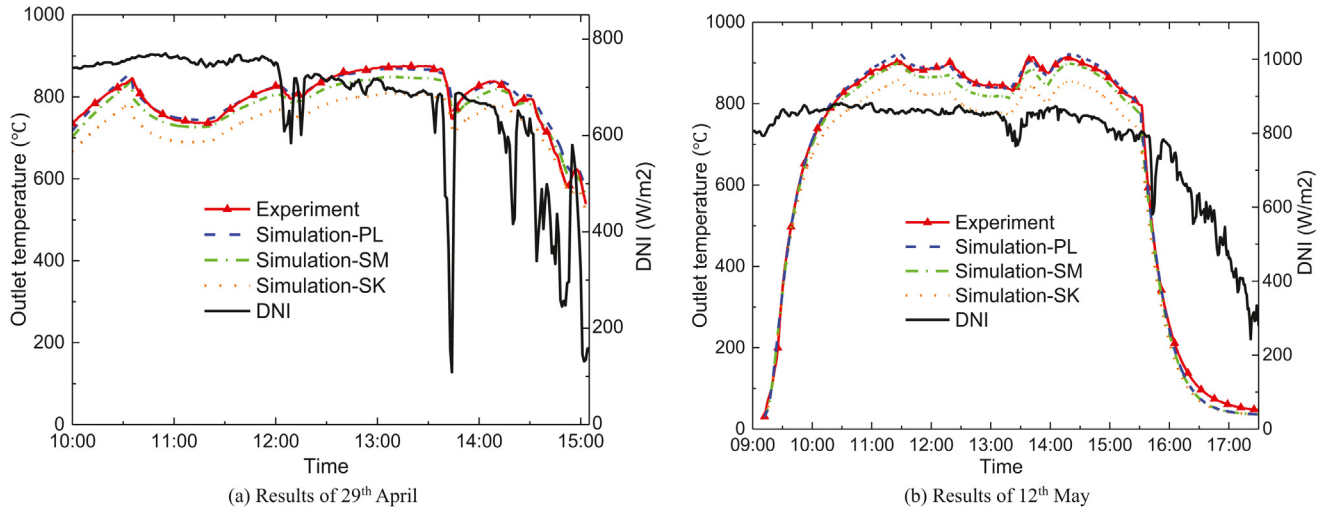


Fig. 13. The comparison of experiment and simulation results with different convection heat loss correlations.

Table 3

RMSE values between experiment and simulation results using different convection heat loss correlations.

RMSE value	Results of 29th April	Results of 12th May
SK equation	7.01%	8.62%
SM equation	2.53%	4.71%
PL equation	1.91%	3.92%

rising value increases from 200 W/m² to 800 W/m². When DNI decreases from 800 W/m² to 0, it takes 623 s for the air receiver outlet temperature to drop below 600 °C. It can provide sufficient time for operation adjustment of solar air Brayton cycle system when DNI fluctuates.

Fig. 14 (b) shows the responses of air receiver outlet temperature for start-up and shut-down periods with heat capacity changes of 0.5 times the initial value, the initial value, 1.5 times the initial value and 2.0 times the initial value. The initial heat capacity of the air receiver is 573.8 kJ/°C. For the initial heat capacity, the temperature changing rates of the receiver outlet for start-up and shut-down

periods are 64.6 °C/min and 41.3 °C/min, respectively. For 2.0 times the initial heat capacity, these values are 33.3 °C/min and 20.6 °C/min. The temperature changing rate is inversely proportional to the receiver heat capacity roughly.

4.3.2. Intraday simulation for the integrated system

Here the intraday simulation of the heliostat field and the air receiver is carried out with different control strategies. The actual DNI data of 12th May is used as the simulation boundary. There are 60 mirrors adopted for the intraday simulation. The heliostat field performance and the receiver performance of simulation are analyzed.

Fig. 15 shows the heliostat field performance on 12th May. The thermal power is the solar energy incident to the receiver. The heliostat field efficiency is the product of cosine efficiency, shading efficiency and blocking efficiency. The interception efficiency is the ratio of thermal power to the total solar energy collected by the heliostat field on the solar tower. During the simulation, the thermal power is fluctuant with DNI changes. The maximum thermal power is about 234.90 kW at 14:05 when DNI is 873 W/m². The

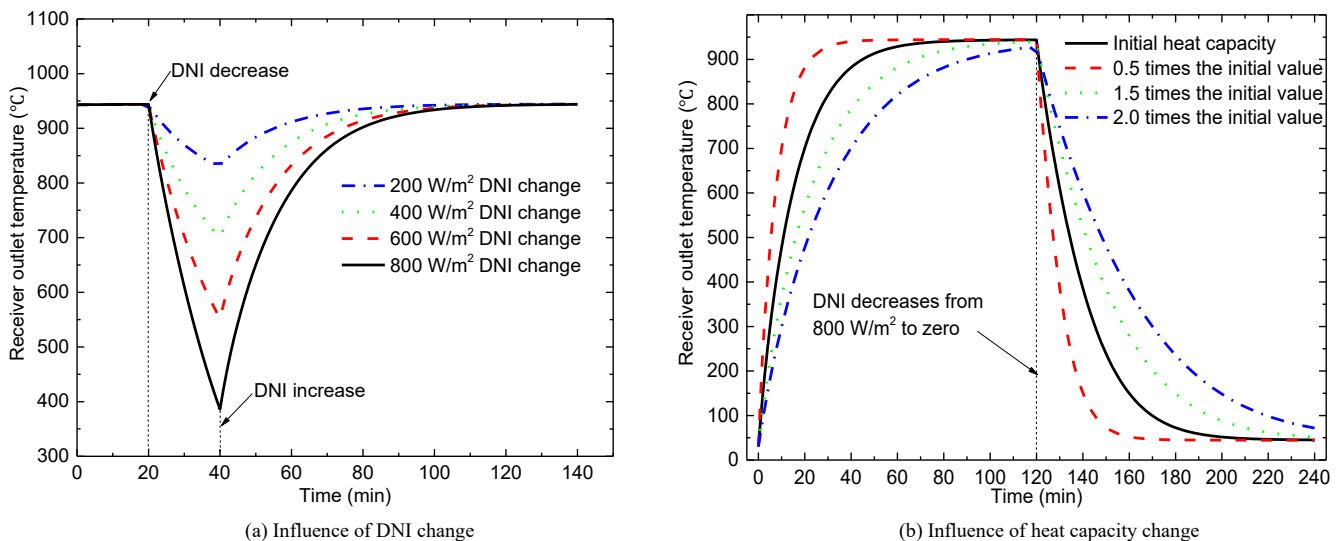


Fig. 14. Dynamic performance of air receiver affected by different factors.

heliostat field efficiency and the interception efficiency are 0.8763 and 0.4453, respectively. At 14:39, the heliostat field efficiency has the highest value of 0.8811, while at 13:15 the interception efficiency has the highest value of 0.4493.

Two cases of air receiver simulation are compared here: the intraday simulation with a constant mass flow rate (0.16 kg/s) and the intraday simulation with a constant outlet temperature (800 °C). The constant-outlet-temperature operation strategy of the air receiver is achieved by using a PI controller to adjust the mass flow rate. The comparison results of the two cases are shown in Fig. 16. When the air receiver operates in the constant-mass-flow-rate strategy, the receiver power and the receiver outlet temperature fluctuate with DNI changes. The maximum receiver outlet temperature and receiver power are 866 °C and 146 kW, respectively.

When the solar receiver operates in the constant-outlet-temperature strategy, the mass flow rate of the air receiver keeps in a low value to increase the receiver outlet temperature rapidly at first. When the receiver outlet temperature reaches above 800 °C, the PI controller works to adjust the mass flow rate. In this way, the receiver outlet temperature can be kept around 800 °C. The maximum receiver power is 158 kW in this case. From the simulation results, it is known that the constant-outlet-temperature case has a shorter time (about 111 min) for receiver temperature reaching 800 °C. This control strategy is more suitable for fast start-up. While for the constant-mass-flow-rate case, this time is near 6 h (355 min). However, the total thermal energy absorbed by the air receiver is 1086 kWh for the constant-outlet-temperature case, this value is 1216 kWh for the constant-mass-flow-rate case.

5. Conclusions

In this work, a solar tower collector system for solar power generation was constructed and the experiment was carried out. An integrated dynamic simulation model consisted of heliostat field and air receiver sub-models was developed with experimental validation. The main outcomes of this study can be summarized as follows:

- (1) During the heliostat field test, the maximum flux density reflected by 52 mirrors is 388 kW/m² when DNI is 750 W/m². The relative errors of the maximum flux density and the total collected solar energy between experiment and simulation are 3.81% and 3.05%.

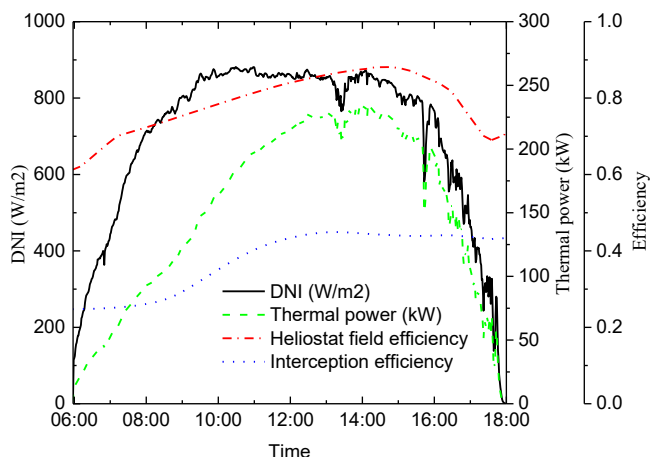


Fig. 15. The heliostat field performance of 12th May for 40 mirrors.

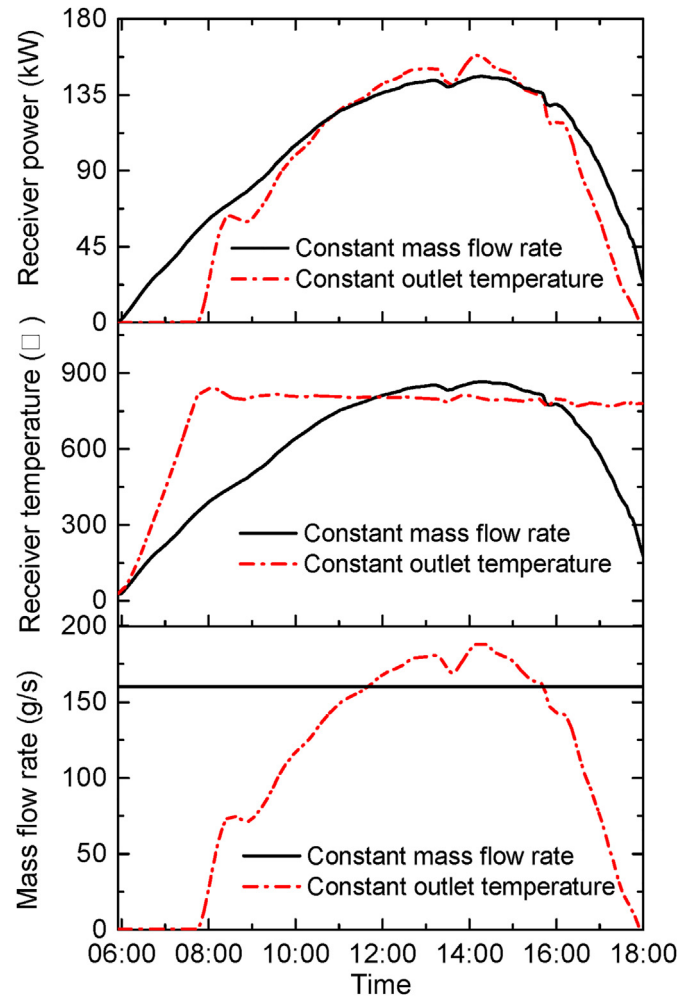


Fig. 16. The comparison results of two cases.

- (2) During the receiver test, the receiver outlet temperature can reach above 880 °C. The pressure loss inside the air receiver is 0.88% when the inlet pressure is above 280 kPa. The maximum thermal efficiency and the maximum thermal power of the air receiver can reach 68.9% and 132 kW, respectively.
- (3) The pressure loss inside the air receiver has a quicker response than the receiver outlet temperature when the mass flow rate changes. The temperature dropping rate for the air receiver is much faster than its temperature rising rate when DNI changes. A more accurate equation to calculate the convection heat loss of the air receiver is determined by comparing with the experimental data.
- (4) During an intraday simulation the constant-outlet-temperature operation strategy of the air receiver is more suitable for fast start-up while the constant-mass-flow-rate operation strategy absorbs much more solar energy.

Further work should concentrate on the improvement of the air receiver model, considering of radiation transfer process among the receiver tubes and the effect of ambient wind on the receiver performance. Also, further work is needed to study and optimize the control strategies of the receiver and heliostat field when coupling with the solar Brayton cycle system.

CRedit authorship contribution statement

Jinli Chen: Methodology, Software, Validation, Formal analysis, Writing – original draft. **Gang Xiao:** Conceptualization, Methodology, Investigation, Resources, Data curation, Writing – review & editing. **Haoran Xu:** Writing – review & editing. **Xin Zhou:** Investigation. **Jiamin Yang:** Investigation. **Mingjiang Ni:** Visualization. **Kefa Cen:** Supervision.

Declaration of competing interest

The authors declare that they have no known competing financial interests or personal relationships that could have appeared to influence the work reported in this paper.

Acknowledgements

The authors gratefully acknowledge the support from the Zhejiang Provincial Natural Science Foundation (No. LR20E060001), the Zhejiang Provincial Key R&D Program (No. 2022C01043) and the Innovative Research Groups of the National Science Foundation of China (No.51621005).

References

- [1] C. Zou, Y. Zhang, Q. Falcoz, P. Neveu, C. Zhang, W. Shu, et al., Design and optimization of a high-temperature cavity receiver for a solar energy cascade utilization system, *Renew. Energy* 103 (2017) 478–489.
- [2] C.J. Winter, R.L. Sizmann, L.L. Vant-Hull, *Solar Power Plants: Fundamentals, Technology, Systems, Economics*, Berlin, 1991.
- [3] F.J. Santos-Alamillos, D. Pozo-Vázquez, J.A. Ruiz-Arias, L. Von Bremen, J. Tovar-Pescador, Combining wind farms with concentrating solar plants to provide stable renewable power, *Renew. Energy* 76 (2015) 539–550.
- [4] Q. Zhang, D. Cao, K. Jiang, X. Du, E. Xu, Heat transport characteristics of a peak shaving solar power tower station, *Renew. Energy* 156 (2020) 493–508.
- [5] J. Ballestrin, A non-water-cooled heat flux measurement system under concentrated solar radiation conditions, *Sol. Energy* 73 (2002) 159–168.
- [6] A. Salomé, F. Chhel, G. Flamant, A. Ferrière, F. Thiery, Control of the flux distribution on a solar tower receiver using an optimized aiming point strategy: application to THEMIS solar tower, *Sol. Energy* 94 (2013) 352–366.
- [7] J.D. Ortega, S.D. Khivarsa, J.M. Christian, P. Dutta, C.K. Ho, On-sun testing of a high temperature bladed solar receiver and transient efficiency evaluation using air, in: *Proceedings of the ASME 12th International Conference on Energy Sustainability*, 2018, 2018.
- [8] P.L. Leary, J.D. Hankins, *User's Guide for MIRVAL: a Computer Code for Comparing Designs of Heliostat-Receiver Optics for Central Receiver Solar Power Plants*, 1979.
- [9] T. Wendelin, SolTRACE- a new optical modeling tool for concentrating solar optics, *Sol. Energy* (2003) 253–260.
- [10] M.J. Blanco, J.M. Amieva, A. Mancilla, The Tonatiuh Software Development Project: an open source approach to the simulation of solar concentrating systems, *Proceedings of the ASME Computers and Information in Engineering Division* (2005) 157–164.
- [11] F. Biggs, C.N. Vittitoe, *The Helios Model for the Optical Behavior of Reflecting Solar Concentrators*, 1979.
- [12] F.J. Collado, A. Gomez, J.A. Turegano, An analytic-function for the flux-density due to sunlight reflected from a heliostat, *Sol. Energy* 37 (1986) 215–234.
- [13] P. Schwarzbözl, M. Schmitz, R. Pitz-Paal, *Visual HFLCAL - A Software Tool for Layout and Optimisation of Heliostat Fields*, SolarPACES, Berlin, 2009.
- [14] A. Sánchez-González, D. Santana, Solar flux distribution on central receivers: a projection method from analytic function, *Renew. Energy* 74 (2015) 576–587.
- [15] F.J. Collado, J. Guallar, Fast and reliable flux map on cylindrical receivers, *Sol. Energy* 169 (2018) 556–564.
- [16] M.R. Rodríguez-Sánchez, A. Sánchez-González, D. Santana, Field-receiver model validation against Solar Two tests, *Renew. Sustain. Energy Rev.* 110 (2019) 43–52.
- [17] M. Atif, F.A. Al-Sulaiman, Optimization of heliostat field layout in solar central receiver systems on annual basis using differential evolution algorithm, *Energy Convers. Manag.* 95 (2015) 1–9.
- [18] T. Ashley, E. Carrizosa, E. Fernández-Cara, Continuous optimisation techniques for optimal aiming strategies in solar power tower plants, *Sol. Energy* 190 (2019) 525–530.
- [19] B. Grange, C. Dalet, Q. Falcoz, A. Ferrière, G. Flamant, Impact of thermal energy storage integration on the performance of a hybrid solar gas-turbine power plant, *Appl. Therm. Eng.* 105 (2016) 266–275.
- [20] C.K. Ho, B.D. Iverson, Review of high-temperature central receiver designs for concentrating solar power, *Renew. Sustain. Energy Rev.* 29 (2014) 835–846.
- [21] A. Kribus, P. Doron, R. Rubin, R. Reuven, E. Taragan, S. Duchan, et al., Performance of the directly-irradiated annular pressurized receiver (DIAPR) operating at 20 bar and 1,200°C, *J. Sol. Energy Eng.* 123 (2001) 10–17.
- [22] A.L. Avila-Marín, Volumetric receivers in solar thermal power plants with central receiver system technology: a review, *Sol. Energy* 85 (2011) 891–910.
- [23] P. Heller, SOLHYCO: Solar-Hybrid Power and Cogeneration Plants, Deutsches Zentrum für Luft- und Raumfahrt, Germany, 2011.
- [24] R. Korzynietz, J.A. Brioso, A. del Río, M. Quero, M. Gallas, R. Uhlrig, et al., Solugas – comprehensive analysis of the solar hybrid Brayton plant, *Sol. Energy* 135 (2016) 578–589.
- [25] Ortega JD, Khivarsa SD, Christian JM, Dutta P, Ho CK. ON-SUN TESTING OF A HIGH TEMPERATURE BLADED SOLAR RECEIVER AND TRANSIENT EFFICIENCY EVALUATION USING AIR. ASME2018.
- [26] C. Zou, Y. Zhang, H. Feng, Q. Falcoz, P. Neveu, W. Gao, et al., Effects of geometric parameters on thermal performance for a cylindrical solar receiver using a 3D numerical model, *Energy Convers. Manag.* 149 (2017) 293–302.
- [27] M. Uzair, T.N. Anderson, R.J. Nates, Modeling of convective heat loss from a cavity receiver coupled to a dish concentrator, *Sol. Energy* 176 (2018) 496–505.
- [28] L. Xu, W. Stein, J.-S. Kim, Z. Wang, Three-dimensional transient numerical model for the thermal performance of the solar receiver, *Renew. Energy* 120 (2018) 550–566.
- [29] J. Samanes, J. Garcia-Barberena, A model for the transient performance simulation of solar cavity receivers, *Sol. Energy* 110 (2014) 789–806.
- [30] L. Xiao, F.-W. Guo, S.-Y. Wu, Z.-L. Chen, A comprehensive simulation on optical and thermal performance of a cylindrical cavity receiver in a parabolic dish collector system, *Renew. Energy* 145 (2020) 878–892.
- [31] S. Soltani, M. Bonyadi, V. Madadi Avargani, A novel optical-thermal modeling of a parabolic dish collector with a helically baffled cylindrical cavity receiver, *Energy* 168 (2019) 88–98.
- [32] S. Pavlovic, A.M. Daabo, E. Bellos, V. Stefanovic, S. Mahmoud, R.K. Al-Dadah, Experimental and numerical investigation on the optical and thermal performance of solar parabolic dish and corrugated spiral cavity receiver, *J. Clean. Prod.* 150 (2017) 75–92.
- [33] E. Bellos, E. Bousi, C. Tzivanidis, S. Pavlovic, Optical and thermal analysis of different cavity receiver designs for solar dish concentrators, *Energy Convers. Manag.* X 2 (2019), 100013.
- [34] Z. Si-Quan, L. Xin-Feng, D. Liu, M. Qing-Song, A numerical study on optical and thermodynamic characteristics of a spherical cavity receiver, *Appl. Therm. Eng.* 149 (2019) 11–21.
- [35] J. Yang, G. Xiao, M. Ghavami, J. Al-Zaili, T. Yang, A. Sayma, et al., Thermodynamic modelling and real-time control strategies of solar micro gas turbine system with thermochemical energy storage, *J. Clean. Prod.* 304 (2021), 127010.
- [36] G. Xiao, K.K. Guo, W.P. Xu, M.J. Ni, Z.Y. Luo, K.F. Cen, An improved method of Lambertian CCD-camera radiation flux measurement based on SMARTS (simple model of the atmospheric radiative transfer of sunshine) to reduce spectral errors, *Energy* 67 (2014) 74–80.
- [37] A. Chinnici, G.J. Nathan, B.B. Dally, Experimental demonstration of the hybrid solar receiver combustor, *Appl. Energy* 224 (2018) 426–437.
- [38] Ortega JD, Christian JM, Ho CK. Design and Testing of a Novel Bladed Receiver. ASME2017.
- [39] F.J. Collado, One-point fitting of the flux density produced by a heliostat, *Sol. Energy* 84 (2010) 673–684.
- [40] S.M. Besarati, D. Yogi Goswami, A computationally efficient method for the design of the heliostat field for solar power tower plant, *Renew. Energy* 69 (2014) 226–232.
- [41] D.L. Siebers, J.S. Kraabel, *Estimating Convective Energy Losses from Solar Central Receivers*, Sandia National Labs., Livermore, CA (USA), 1984, p. 68. Medium: ED; Size.
- [42] W.B. Stine, C.G. McDonald, Cavity receiver convective heat loss, in: *International Solar Energy Society (ISES) Solar World Conference*. Kobe, Japan, 1989.
- [43] S. Paitoonsurikarn, K. Lovegrove, A new correlation for predicting the free convection loss from solar dish concentrating receivers, in: *Proceedings of the Conference of the Australia and New Zealand Solar Energy Society (Solar 2006)*: Australian and New Zealand Solar Energy Society (ANZSES), 2006, p. 9.
- [44] V. Gnielinski, New equations for heat and mass-transfer in turbulent pipe and channel flow, *Int. Chem. Eng.* 16 (1976) 359–368.
- [45] B.S. Petukhov, Heat transfer and friction in turbulent pipe flow with variable physical properties, *Advances in Heat Transfer* 6 (1970) 503–564.

Nomenclature

Latin symbols

- A: area (m²)
 c_p : constant pressure specific heat (J/kgK⁻¹)
 c_v : constant volume specific heat (J/kgK⁻¹)
D: distance/diameter (m)
F: view factor
 f_{at} : atmospheric attenuation factor
Gr: Grashof number

h: heat transfer coefficient ($\text{W/m}^2\text{K}^{-1}$)
I_D: direct normal irradiance (W/m^2)
k: heat conductivity coefficient (W/mK^{-1})
L: length (m)
M: mass (kg)
m: mass flow (kg/s)
n_d: data number
Nu: Nusselt number
P: pressure (kPa)
Pow: power (kW)
Pr: prandtl number
Q: heat power (kW)
q: heat flux (W/m^2)
S: heat exchange area (m^2)
T: temperature ($^{\circ}\text{C}$)
t: time (s)
y: simulation data
y_m: experiment data

Greek symbols

α: angle
β: reflectivity
δ: heliostat cleanliness
ε: emissivity
η: efficiency
ρ: density (kg/m^3)
Φ: inclination
σ: error

φ: Stefan-Boltzmann constant

Abbreviations

CSP: concentrating solar power
DNI: direct normal irradiance (W/m^2)
RMSE: root mean square error

Subscripts

abs: absorb
amb: ambient
AP: aim point
ape: aperture
ast: astigmatic effect of reflected rays
b&s: Blocking and shading
bq: beam quality
cav: cavity
con: convection
in: inlet
ins: thermal insulation layer
inv: inverter
m: mirror
out: outlet
rad: radiation
ref: reflection
sun: sun shape
t: tracking